buildings

MDPI

Article

Research on Deformation Behavior and Mechanisms of Concrete Under Hygrothermal Coupling Effects

Mingyu Li [1,2], Chunxiao Zhang [1,3,4], Aiguo Dang [1,3,4], Xiang He [1,3,4,*], Jingbiao Liu [1,3,4,*] and Xiaonan Liu [1,5]

[1] Defense Engineering Institute, AMS, PLA, Luoyang 471023, China; 18817261953@163.com (M.L.); zhangchunxiaocivil@163.com (C.Z.); aigo_d@163.com (A.D.); liuxiaonan@hrbeu.edu.cn (X.L.)
[2] School of Intelligent Construction and Civil Engineering, Luoyang Institute of Science and Technology, Luoyang 471023, China
[3] State Key Laboratory of Target Vulnerability Assessment, Luoyang 471023, China
[4] Henan Key Laboratory Special Protective Materials, Luoyang 471023, China
[5] College of Aerospace and Civil Engineering, Harbin Engineering University, Harbin 150001, China
* Correspondence: xianghe1396@163.com (X.H.); liujingbiao@hrbeu.edu.cn (J.L.)

Abstract

This study elucidated the evolution and catastrophic failure mechanisms of concrete's mechanical properties under high-temperature and moisture-coupled environments. Specimens underwent hygrothermal shock simulation via constant-temperature drying (100 °C/200 °C, 4 h) followed by water quenching (20 °C, 30 min). Uniaxial compression tests were performed using a uniaxial compression test machine with synchronized multi-scale damage monitoring that integrated digital image correlation (DIC), acoustic emission (AE), and infrared thermography. The results demonstrated that hygrothermal coupling reduced concrete ductility significantly, in which the peak strain decreased from 0.36% (ambient) to 0.25% for both the 100 °C and 200 °C groups, while compressive strength declined to 42.8 MPa (−2.9%) and 40.3 MPa (−8.6%), respectively, with elevated elastic modulus. DIC analysis revealed the temperature-dependent failure mode reconstruction: progressive end cracking (max strain 0.48%) at ambient temperature transitioned to coordinated dual-end cracking with jump-type damage (abrupt principal strain to 0.1%) at 100 °C and degenerated to brittle fracture oriented along a singular path (principal strain band 0.015%) at 200 °C. AE monitoring indicated drastically reduced micro-damage energy barriers at 200 °C, where cumulative energy (4000 mV·ms) plummeted to merely 2% of the ambient group (200,000 mV·ms). Infrared thermography showed that energy aggregation shifted from "centralized" (ambient) to "edge-to-center migration" (200 °C), with intensified thermal shock effects in fracture zones ($\Delta T \approx -7.2$ °C). The study established that hygrothermal coupling weakens the aggregate-paste interfacial transition zone (ITZ) by concentrating the strain energy along singular weak paths and inducing brittle failure mode degeneration, which thereby provides theoretical foundations for fire-resistant design and catastrophic failure warning systems in concrete structures exposed to coupled environmental stressors.

Keywords: fire; hygrothermal coupling; DIC (digital image correlation); acoustic emission (AE); thermal infrared

check for updates

Academic Editors: Cedric Payan and Jian-Guo Dai

Received: 26 August 2025
Revised: 12 September 2025
Accepted: 15 September 2025
Published: 29 September 2025

Citation: Li, M.; Zhang, C.; Dang, A.; He, X.; Liu, J.; Liu, X. Research on Deformation Behavior and Mechanisms of Concrete Under Hygrothermal Coupling Effects. *Buildings* **2025**, *15*, 3514. https://doi.org/10.3390/buildings15193514

Copyright: © 2025 by the authors. Licensee MDPI, Basel, Switzerland. This article is an open access article distributed under the terms and conditions of the Creative Commons Attribution (CC BY) license (https://creativecommons.org/licenses/by/4.0/).

1. Introduction

The coupled temperature–humidity environment created by high fire temperatures and fire sprinklers has a significant effect on accelerating the degradation of concrete

structures' performance [1,2]. Under the combined action of high fire temperatures and rapid cooling, complex physical and chemical processes occur within concrete: the cement gel undergoes dehydration and shrinkage, the aggregate-paste interface transition zone (ITZ) is weakened, and the abrupt change in vapor pressure attributable to moisture infiltration and thermal shock effects induce the further propagation of microcracks [3–5]. Studies have shown that the degree of damage in concrete cooled by sprinklers after a fire is more than 40% higher than that exposed to high temperature alone, and its core mechanism involves thermo-mechanical–hygro-chemical multi-field coupling [6,7]. Particularly in the temperature range of 100–200 °C, the reconstruction of energy dissipation patterns dominated by the latent heat of the water phase change and the Joule–Thomson effect has become a key blind spot in predicting catastrophes [8,9]. Revealing the deformation mechanisms and damage evolution laws of concrete in such environments is of urgent engineering significance to improve the fire resistance of building structures and assess post-disaster safety.

Current research on concrete's high-temperature performance focuses primarily on three directions: With respect to pure high-temperature effects, the strength–temperature models that Khoury and Schneider established [10] (such as the ISO 834 standard curve) ignore the influence of humidity migration and lead to a deviation of 15–20% in predicting strength under sprinkler cooling conditions. With respect to thermo-hygro coupling theory, although Gawin's porous-medium model can describe moisture transport, it lacks experimental verification of interface damage evolution. Domestic scholars have observed the propagation of ITZ microcracks through SEM, but failed to quantify the rate at which they contribute to macroscopic mechanical properties [11,12]. With respect to damage monitoring technology, the application of DIC, AE, and infrared technology has obvious limitations: DIC is insufficiently accurate in reconstructing the high-temperature full-field strain field (error > 0.1%) [13,14], AE lags in early warning of brittle transition under temperature–humidity coupling, and infrared thermography focuses largely on absolute temperature values while it ignores gradient inversion attributable to the latent heat of phase change (such as the "high-temperature core–low-temperature ring" feature). However, existing studies focus on high temperatures above 400 °C or normal temperature–humidity fields and lack experimental data on temperature–humidity coupling in the 100–300 °C range where cement hydration undergoes drastic changes; further, the evolution of microcracks (AE), strain localization (DIC), and thermodynamic responses (infrared) have not been correlated synchronously [15], which makes it difficult to establish a multi-scale damage constitutive model. Finally, the forward shift phenomenon of the brittle failure threshold caused by interface weakening lacks quantitative description [16–18].

This study overcomes the above limitations through an innovative experimental system: constructing 100/200 °C constant-temperature drying and 20 °C water-cooled thermal–humidity shock sequences to simulate fire sprinkler conditions, using a DRTB-4000 uniaxial compression test machine to achieve highly precise uniaxial compression (0.5 MPa/s), integrating DIC (Vic-3D system, spatial resolution 0.5 mm), AE (PAC PCI-2, positioning accuracy ± 2 mm), and infrared thermography (Imager SX) technologies synchronously to realize multi-scale dynamic tracking of damage. This system revealed the law of failure mode reconstruction induced by ITZ weakening (progressive failure with multiple cracks at room temperature, jump-type damage at 100 °C, and single-path brittle fracture at 200 °C); identified the thermal shock strengthening mechanism dominated by the latent heat of vapor phase change and Joule–Thomson effect ($\Delta T \approx -7.2$ °C); established a quantitative model of the "strain energy concentration–brittle degradation index", and clarified the degradation criterion of the displacement field from composite type to unidirectional separation. These achievements provide a new theoretical tool to design a

fire protection and early catastrophic failure warning system of concrete structures in high-temperature and high-humidity environments, such as nuclear power plant containment structures and undersea tunnels.

2. Materials and Methods

2.1. Experimental Materials and Instruments

2.1.1. Experimental Materials

The materials employed include P42.5 Portland cement (manufactured by Hubei Zhongxia Cement (Group) Co., Ltd. in Jingmen, China), coarse aggregate consisting of granite crushed stone with a diameter ranging from 5 mm to 25 mm, fine aggregate in the form of quartz sand (characterized by medium sand gradation, a fineness modulus of 2.6, an apparent density of 2630 kg/m^3, and a mud content of less than 1.0%), purified water as the water component, a polycarboxylate high-performance water-reducing agent (branded as Jiangsu Sobute, model PCE-100, produced by Jiangsu Sobute New Materials Co., Ltd., in Nanjing, China, with a solid content of 20% and a water reduction rate of no less than 30%) serving as the water-reducing agent, and polypropylene (PP) fibers (manufactured by Jiangsu Fasten New Materials Technology Co., Ltd., in Jiangyin, China, model FSPP-6, featuring a length of 6 mm, a diameter of 20 μm, a tensile strength of at least 550 MPa, an elastic modulus of no less than 3.5 GPa, and an elongation at break ranging from 15% to 30%).

2.1.2. Experimental Instruments

A DRTB-4000 electro-hydraulic servo rock uniaxial compression test machine, Imager SX series 5MP, CCD camera, acoustic emission system, and thermal infrared system were used. The test instruments are shown in Figure 1.



Figure 1. Experimental setup.

In the study on the mechanical properties and damage mechanisms of concrete under the coupling effect of temperature and humidity, the DRTB-4000 electro-hydraulic servo rock uniaxial compression test machine (manufactured by Jilin Province Huaxing Testing Machine Co., Ltd., Changchun, China) provides loading conditions for obtaining mechanical parameters (such as stress–strain curves and compressive strength) by applying uniaxial compressive loads and precisely controlling the loading rate (0.5 MPa/s) and load. Meanwhile, the FLIR Imager SX infrared thermal imager (produced by FLIR Systems, Inc., Wilsonville, OR, USA) conducts synchronous infrared thermal imaging tests, which involve real-time collection of temperature field distribution data on the surface of concrete

specimens and capture of thermal shock effects related to cracks (e.g., ΔT changes), so as to analyze the thermodynamic response and energy dissipation law of concrete under temperature–humidity coupling. The CCD camera (equipped with fill lights; model and manufacturer depend on specific configuration, though common examples include PCO GmbH, Kelheim, Germany or FLIR Systems, Inc., USA), serving as the core imaging device for the digital image correlation (DIC) test, acquires speckle images of the specimen surface under stable illumination provided by the fill lights; combined with the Vic-3D system, it calculates the full-field displacement and strain, thereby revealing the deformation characteristics and evolution of failure modes of concrete. Additionally, the acoustic emission (AE) sensors (components of the AE system), attached to the surface of concrete specimens, capture in real time the AE signals generated by the initiation and propagation of internal microcracks. Through the analysis of signal parameters (e.g., cumulative energy and event frequency) via the PAC PCI-2 AE system, they facilitate the investigation into the evolution mechanism of microscopic damage and the variation law of energy barriers.

2.2. Sample Preparation

Standard cubic concrete specimens with dimensions of 100 mm × 100 mm × 100 mm were prepared according to the mix proportion in Table 1. They were formed by mechanical vibration compaction, demolded after 24 h of static curing (see Figure 2), and then placed in a standard curing room with a temperature of (20 ± 2) °C and a relative humidity of ≥95% and were cured for 28 days [19–21]. After the curing period, the specimens were divided systematically into three groups, each of which contained three parallel specimens. The first group was the normal-temperature control group (numbered CW-1, CW-2, CW-3), which was kept in the standard environment throughout without additional treatment; the second group was subjected to 100 °C heat treatment (numbered 100-1, 100-2, 100-3), and the specimens were placed in a constant-temperature oven, heated to 100 °C at a rate of 5 °C/min, and then kept at a constant temperature for 4 h; the third group was subjected to 200 °C heat treatment (numbered 200-1, 200-2, 200-3) and heated to 200 °C according to the same heating procedure and kept at a constant temperature for 4 h. After the high-temperature treatment, the specimens in the second and third groups were transferred immediately to a constant-temperature water bath preset to 20 °C for 30 min of immersion cooling to simulate the coupling effect of a rapid drop in temperature and humidity. Among them, the 4 h heating period for Group 2 and Group 3 was designed in accordance with the relevant guiding principles for high-temperature performance tests specified in the national standard GB/T 50082-2009 "Standard for Test Methods of Long-Term Performance and Durability of Ordinary Concrete". The 330 min cooling duration was adopted based on the methods described in References [19,22]; this cooling period was designed according to the results of preliminary pre-tests, as it can generate a significant temperature gradient inside the test specimens, thereby effectively inducing microcracks caused by severe thermal shrinkage. This is also a commonly used method for studying the thermal shock resistance of concrete and the damage mechanism of concrete after exposure to high temperatures followed by cooling (see Figure 3) [22,23].

Table 1. Concrete mix proportions.

Cement (kg)	Water (kg)	Sand (kg)	Stone (kg)	PP Fiber (kg)	Water Reducer (kg)
0.272	0.122	0.476	0.748	0.001	0.0136

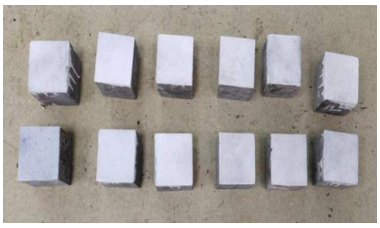

Figure 2. Specimens.



Figure 3. Water quenching setup (20 °C).

2.3. Test and Measurement

2.3.1. Uniaxial Compression Test Method

Uniaxial compression tests were carried out in accordance with the specification requirements within 2 h after the concrete specimens subjected to temperature–humidity coupling pretreatment were removed from the water bath.

2.3.2. DIC Testing

A dual-camera digital image correlation (DIC) system triggered synchronously with the mechanical testing machine was used to measure the full-field deformation on the specimens' surface. Random speckles were prepared on the surface of the specimens, and a highly precise stereo calibration was performed before loading (reprojection error < 0.02 pixels). The experiment was loaded in a displacement-controlled mode (0.2 mm/min) under a constant temperature and in a vibration-isolated environment, with synchronous acquisition of images (1 Hz) and load data. DIC calculation was based upon the assumption of gray-scale conservation, and the speckle displacement was tracked by the inverse compositional Gauss–Newton (IC-GN) algorithm with sub-pixel accuracy. The calculation principle was to maximize the zero-mean normalized cross-correlation (ZNCC) coefficient between the target sub-region and the reference sub-region.

$$ZNCC = \frac{\sum\left[\left(f(x,y) - \overline{f}\right) \cdot \left(g(x',y') - \overline{g}\right)\right]}{\sqrt{\sum\left(f(x,y) - \overline{f}\right)^2} \cdot \sqrt{\sum(g(x',y') - \overline{g})^2}} \quad (1)$$

2.3.3. Acoustic Emission Testing

The DIC system measured the full-field displacement and strain on the specimens' surface synchronously.

2.3.4. Infrared Measurement

First, the cured concrete specimens were placed in a constant-temperature environmental chamber (23 ± 0.5 °C) for 2 h to stabilize thermal equilibrium. Then, a matte black paint (emissivity ε = 0.95) was sprayed uniformly on the specimens' surface to ensure uniform emissivity. Before the formal test, the Imager SX infrared thermal imager (thermal sensitivity 0.03 °C) was calibrated on-site with a built-in blackbody radiation source (accuracy ± 0.1 °C) [24–26]. The sampling frequency was set to 1 Hz and the spatial resolution

to 3 mm, and the thermal imager's optical axis was aligned vertically with the center of the specimen (at a distance of 50 cm). The DRTB-4000 testing machine was started and applied a uniaxial compressive load at a rate of 0.5 MPa/s, while the infrared system was triggered synchronously to collect thermal image sequences continuously [11,27,28]. During the loading process, the ambient temperature and humidity were monitored in real time (compensation parameters were recorded), and the device clock synchronization was maintained (error < 0.1 s) [29–31]. After loading, the original thermal images were subjected to non-uniformity correction (NUC) and spatiotemporal filtering. The full-field temperature matrix data were extracted, with a focus on analyzing the temperature change curves (ΔT) and gradient distributions (ΔT) in characteristic regions (such as indenter contact zones and crack initiation zones). Combined with the load–time curve, anomalous thermal events (such as a sudden temperature drop of −7.2 °C attributable to crack propagation) were marked, and finally, temperature field evolution nephograms and time-series thermodynamic response datasets were generated [32,33].

3. Test Results and Analysis

3.1. Uniaxial Compression Test

The uniaxial compressive stress–strain curves under three working conditions (normal temperature, 100 °C, and 200 °C) are shown in Figure 4.

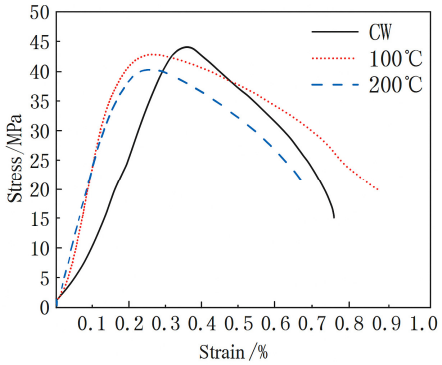

Figure 4. Stress–strain curves.

Based upon the uniaxial compressive stress–strain curves of concrete shown in Figure 4, this study revealed systematically the evolution laws and intrinsic deterioration mechanisms of concrete's mechanical properties at room temperature (~25 °C) and after undergoing temperature–humidity coupling (thermal–humidity treatment) at 100 °C and 200 °C. The test data showed clearly that the room-temperature concrete exhibited the typical characteristics of quasi-brittle materials, with a peak stress of 44.1 MPa and a corresponding peak strain of 0.36%. Before they reached their peak strength, the stress and strain were in an approximately linear proportional relationship, indicating that the material was in the elastic working stage, and the accumulation of microstructural damage was limited. After undergoing 100 °C temperature–humidity coupling, the concrete's peak stress was 42.8 MPa, which is only approximately 2.9% lower than that at room temperature, but its corresponding peak strain decreased significantly to 0.25%, with a drop of up to 30.6%. After 200 °C temperature–humidity coupling, the peak stress decreased further to 40.3 MPa (approximately 8.6% lower than that at room temperature), while the peak strain remained at the low level of 0.25%.

Analysis of the test phenomena showed that the evolution of concrete's mechanical properties under the action of temperature–humidity coupling was attributable largely to the phased characteristics of its internal microstructure deterioration. Under the 100 °C temperature–humidity action, the evaporation of free water within the concrete generated

pore pressure, which induced the propagation of microcracks and weakened the interfacial transition zone (ITZ) between the cement paste and aggregate, which reduced the material's ductility significantly (the peak strain dropped sharply by 30.6%). At this time, the cement hydration products had not decomposed on a large scale, and the aggregate structure was basically intact, so that the loss of compressive strength was limited (only 2.9%). When the temperature rose to 200 °C, the high temperature promoted the dehydration and shrinkage of cement gel, decomposing the C-S-H gel in part, and the difference in thermal expansion between the aggregate and the paste aggravated ITZ damage, which led to a further decrease in strength (8.6%). However, as the concrete's brittle failure mechanism had been formed significantly at the previous 100 °C (the microcrack network was developed widely), the material's deformation capacity dropped to a low-value platform, so the peak strain no longer decreased significantly; this showed the deterioration law in which the strength continues to decay while the brittleness tends to be stable. Among them, the peak strain decreased significantly from 0.36% to 0.25%, while the compressive strength only decreased by 2.9–8.6%. The reason why the strength loss was significantly lower than the ductility loss lies in the following: the temperature–humidity coupled environment first and primarily deteriorates the ductility of concrete. The mechanism behind this is the weakening of the interfacial transition zone (ITZ) and the initiation of microcracks, which is directly manifested as a significant reduction in peak strain. In contrast, the attenuation of compressive strength depends more on the strength of the cement paste matrix itself. Since the cement paste matrix maintains relative integrity in environments below 200 °C, the magnitude of strength loss is smaller than that of ductility loss. This phenomenon of "strength–toughness decoupling" is a typical characteristic of concrete under the combined action of heat and humidity in the medium-temperature range.

3.2. Analysis of Concrete DIC Results

The DIC test results of the specimens under the normal-temperature condition are shown in Figure 5, those under the 100 °C condition are shown in Figure 6, and those under the 200 °C condition are shown in Figure 7.

Figure 5 reveals the meso-mechanical mechanism and progressive failure characteristics of its uniaxial compressive failure. In the initial loading stage (120 s, Figure 5a), the strain concentration appeared in the end region ① of the specimen (local strain 0.0125%), and the displacement field was dominated by horizontal leftward movement that reflected the stress concentration effect caused by end friction constraint. As the load increased (220 s, Figure 5b), the downward component of the displacement vector increased significantly, indicating that axial pressure had begun to dominate the deformation behavior, while the strain distribution remained relatively uniform (maximum strain approximately 0.006%), with the material in the stage of elastic coordinated deformation. In the middle and later stages (320 s, Figure 5c), the emergence of new strain concentration zones ② (0.018%) and ③ (0.006%) marked a qualitative change in the accumulation of internal damage. The continuous increase in the downward component of the displacement field revealed the non-uniform initiation of microcracks at the aggregate–paste interface. When the peak load was approached (436 s, Figure 5d), the strains in zones ② and ③ increased sharply (>0.06% and 0.024%) and formed penetrating microcracks. The displacement field shifted overall to be dominated by the vertical direction, while the displacement vectors in the crack zones showed a horizontal separation trend, which thus confirmed the crack surfaces' tensile–shear composite failure mechanism. In the final failure stage (441 s, Figure 5e), the strains in the main cracks ② and ③ increased suddenly to 0.48%, and secondary cracks ④ and ⑤ developed synchronously (strain 0.12%). The displacement field showed signif-

icant divergence characteristics in the crack regions (e.g., leftward at ② and ③, oblique separation at ④).

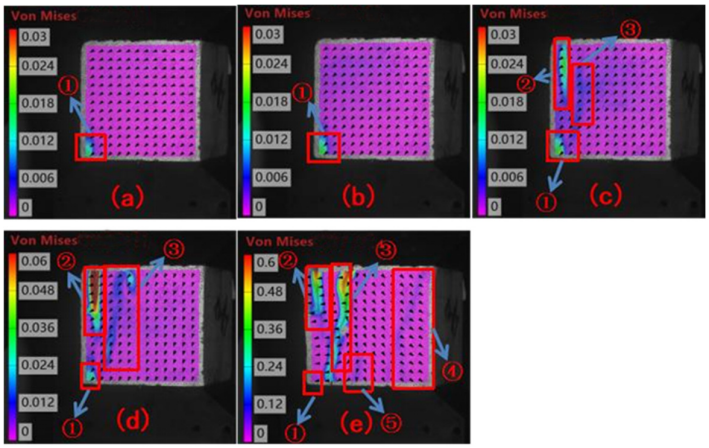

Figure 5. Strain distribution in concrete specimen at ambient temperature ((**a**) 120 s, (**b**) 220 s, (**c**) 320 s, (**d**) 436 s, (**e**) 441 s).

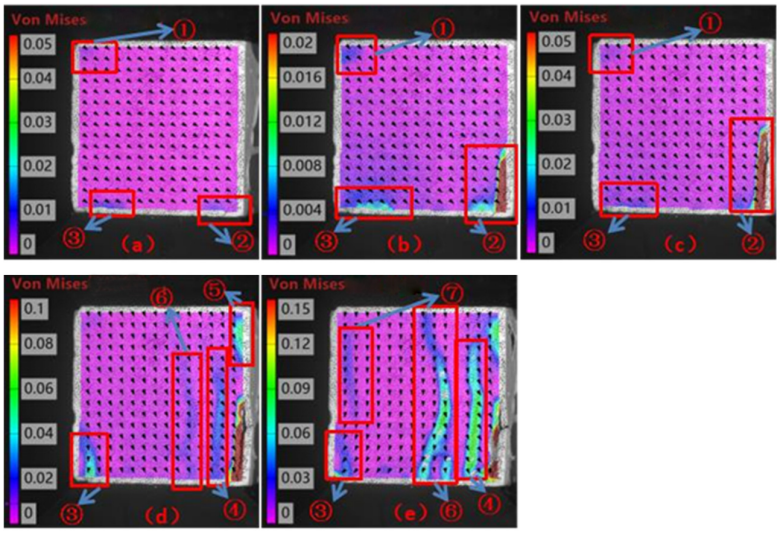

Figure 6. Strain distribution in hygrothermal-conditioned concrete specimen (100 °C) ((**a**) 120 s, (**b**) 220 s, (**c**) 320 s, (**d**) 438 s, (**e**) 448 s).

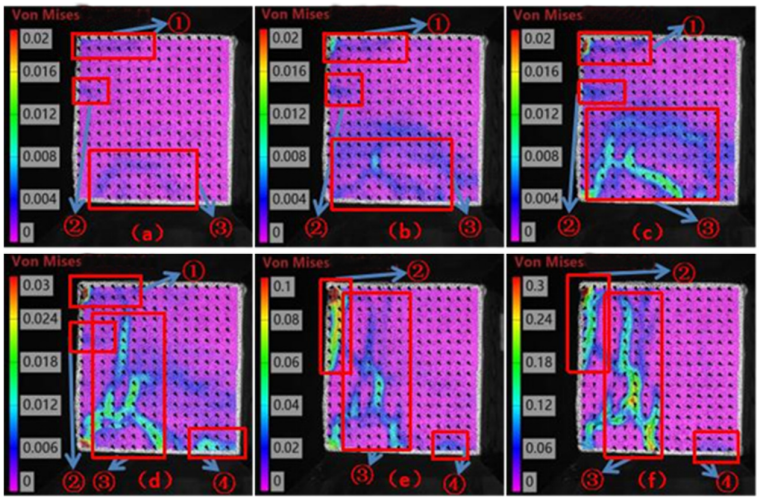

Figure 7. Strain field in concrete specimen after 200 °C hygrothermal exposure (DIC): technical rationale ((**a**) 122 s, (**b**) 220 s, (**c**) 320 s, (**d**) 411 s, (**e**) 439 s, (**f**) 447 s).

Based upon the DIC strain evolution analysis of the 100 °C temperature–humidity-coupled concrete specimen shown in Figure 6, its uniaxial compressive failure process exhibited significantly different modes of damage accumulation and failure compared to the room-temperature specimen. In the initial loading stage (120 s, Figure 6a), strain concentrations (approximately 0.002%) appeared in the end regions ① and ② of the specimen simultaneously, and the displacement field showed a 45° oblique distribution (dominated by the lower left direction) and revealed that the weakening of the interface transition zone caused by temperature–humidity coupling intensified the end constraint effect. As the load increased (Figure 6b 220 s), the main strain concentration zone shifted to the middle region ③ (0.002%) accompanied by increased strain in region ① (0.006%). The downward component of the displacement vector enhanced significantly while the horizontal component remained, which indicated that microcracks initiated preferentially in pre-damaged areas under the dominance of axial pressure. A critical turning point occurred in the middle and later stages (Figure 6c 320 s), where a new strain concentration zone ④ appeared suddenly and the strain values jumped to 0.04% (far exceeding 0.004% in region ③ during the same period). The vertical component of the displacement field continued to increase, indicating that the pre-existing microcrack network within the material promoted the jump-style development of damage. When failure was approached (Figure 6d 392 s), the strain in region ④ surged to 0.06% and formed a penetrating main crack. The displacement field shifted completely from oblique to vertical dominance, and the displacement vectors in the crack zone showed unidirectional leftward expansion characteristics, confirming that the aggregate–paste interface debonding caused by high-temperature and humidity weakened the crack surfaces' shear resistance capacity significantly. In the final failure stage (Figure 6e 412–425 s), the strain of the main crack ④ exceeded 0.1%, and the secondary crack ⑤ developed accordingly (strain 0.02%). The displacement field showed intense horizontal separation in the crack zone (leftward in region ④, rightward in other regions).

The full-field strain evolution analysis of the 200 °C temperature–humidity-coupled concrete specimen during uniaxial compression is presented in Figure 7. In the initial stage (Figure 7a), it exhibited non-uniform deformation dominated by the end effect and formed strain concentration zones of approximately 0.004% at positions ①, ②, and ③, with displacement vectors distributed downward and to the right, indicating the end stress concentration effect in the structure's uncracked state. As the load increased (Figure 7b), the strain at ③ increased significantly to 0.007% and formed a main strain band, while microcracks initiated at ①, and the rightward trend of the displacement field intensified, indicating that local damage had caused a deviation in the deformation path. In Figure 7d, the strain at ③ surged to 0.015%, the crack propagated upward and formed a tendency to penetrate, and the displacement vector maintained the right–down direction, but the crack zone showed rightward expansion, confirming that the main crack dominated the deformation mode. The entire process showed the progressive law: initial strain concentration at the ends (Figure 7a), strain strengthening and microcrack initiation at ③ (Figure 7b), directional propagation of the main crack, and strain localization (Figure 7d). The displacement field changed gradually from the initial uniform sinking to crack-driven rightward expansion. This deformation sequence indicated that the temperature–humidity coupling effect weakened the concrete's coordinated deformation capacity significantly and promoted the concentration of strain energy in specific paths (such as ③), and ultimately triggered the directional propagation of penetrating cracks and the reconstruction of the displacement field, which provides key experimental evidence of concrete structures' catastrophic failure mechanism in high-temperature and high-humidity environments.

The analysis of the concrete's failure mechanism under uniaxial compression based upon DIC technology showed that the specimens under normal-temperature, 100 °C and

200 °C temperature–humidity coupling environments exhibited significantly different damage evolution laws and failure modes. The normal-temperature specimen initially showed horizontal displacement-dominated strain concentration (0.0125%) attributable to end friction constraints, then underwent an elastic coordinated deformation stage (maximum strain 0.006%), and finally was characterized by the progressive propagation of multiple cracks (main crack strain 0.48%) and tensile–shear composite failure. However, because the aggregate–paste interface weakened, the 100 °C temperature–humidity-coupled specimen initially formed an oblique displacement field synchronously at both ends (strain 0.002%). In the middle and later stages, jump-like damage occurred—the strain in the new zone ④ increased suddenly from 0.004% to 0.04%, and the main crack propagated as a one-way left separation (strain exceeded 0.1%), revealing that interface debonding led to the loss of shear resistance. The 200 °C condition exacerbated this trend further: the initial multi-end strain concentration (≈0.004%) locked the main failure path directly (zone ③), the strain band continued to strengthen to 0.015% and expanded directionally to the right, and the displacement field was reconstructed from uniform sinking to crack-driven rightward expansion, which reflected the complete loss of coordinated deformation capacity at high temperatures. Comprehensive analysis showed that as the temperature increased, the concrete degenerated gradually from the multi-crack progressive failure mechanism at normal temperature to the single-crack jump failure at 100 °C, and finally evolved into the directional penetration failure of a single path at 200 °C. The root cause is that the temperature–humidity coupling environment weakened the interface transition zone continuously, which promoted the concentration of strain energy in a single weak zone, and at the same time, the displacement field characteristics degenerated from the composite type (horizontal–vertical coupling at normal temperature) to pure tension dominance (one-way separation at high temperature). This finding warns us that in high-temperature and high-humidity engineering environments, it is necessary to focus on monitoring the end constraint effect and the sudden change in the dominant strain band's behavior, and improve concrete structures' disaster resistance through interface strengthening strategies.

3.3. Acoustic Emission Test

The acoustic emission test results of the specimens under the normal-temperature condition are shown in Figure 8, those under the 100 °C condition are shown in Figure 9, and those under the 200 °C condition are shown in Figure 10.

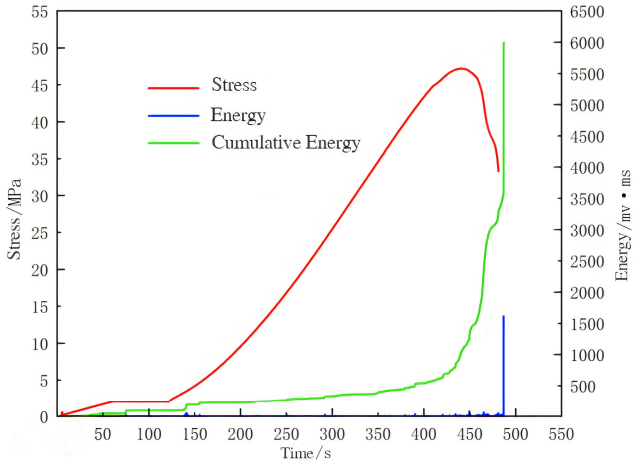

Figure 8. Stress vs. acoustic emission energy in ambient-temperature concrete specimen: technical rationale.

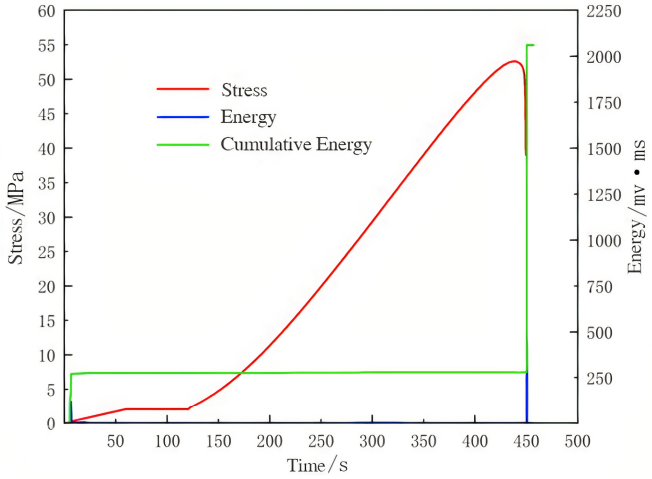

Figure 9. Stress vs. acoustic emission energy in concrete specimen under 100 °C hygrothermal conditioning.

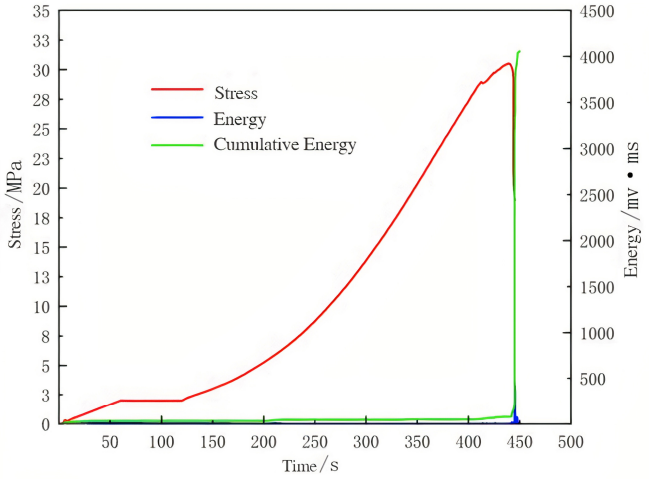

Figure 10. Stress vs. acoustic emission energy in concrete specimen under 200 °C hygrothermal exposure.

The experimental data in Figure 8 indicate clearly that the concrete generated AE signals continuously throughout the loading process. The initiation and propagation of microcracks are inherent characteristics of concrete's response under load, and there was a significant accumulation of microscopic damage even in the macroscopic linear elastic stage. The AE energy release rate showed a strong positive correlation with the stress level applied: in the low-stress stage, energy release was relatively sparse and weak and corresponded to local adjustments of isolated micro-defects within the material; as the stress level approached the peak (approximately 70–80% of the ultimate strength), both the frequency of AE events and the intensity of energy released exhibited a non-linear accelerating growth trend, in which a steep inflection point appeared in the cumulative energy curve. This marked a critical stage where microcracks evolved gradually from relatively stable, dispersed, and independent propagation to densification, interaction, and finally connection to form dominant macroscopic cracks. The surge in cumulative energy, particularly in the section after the peak stress, reflected the enormous fracture energy consumed by the rapid unstable propagation of the crack network.

The analysis of acoustic emission (AE) responses during uniaxial compression of the 100 °C temperature–humidity-coupled concrete specimen in Figure 9 indicated that high-temperature and high-humidity pretreatment altered its damage evolution mechanism and mechanical properties significantly. Although AE activities accompanied the entire

loading process (which confirmed the continuous initiation and propagation of cracks), the characteristics of energy release showed critical changes: at relatively low stress levels, both the frequency of AE events and the intensity of energy release increased significantly, and the cumulative energy curve exhibited an accelerating inflection point before the peak stress was reached. This suggests that temperature–humidity coupling effects (such as microcrack induction, ITZ weakening, or decomposition of hydration products) cause substantial initial damage that reduces the energy barrier required for stable propagation of microcracks significantly, and leads to an earlier threshold and an accelerated rate of damage accumulation. It is noteworthy that the increase in post-peak cumulative energy slowed, implying an increase in the material's brittle tendency, where the crack network tended to concentrate and penetrate more rapidly, and thus reduced post-peak dispersed energy dissipation. In summary, 100 °C temperature–humidity degradation exacerbated the initial sensitivity to damage and the concrete's potential embrittlement, but the failure process still began under low stress, underwent progressive accumulation, and led eventually to instability. These modulated AE characteristics provide key indicators with which to monitor non-destructive damage and assess concrete structures' life in harsh environments.

In the 200 °C condition (Figure 10), the energy release pattern of the specimen exhibited further deterioration compared to the 100 °C condition: at an extremely low stress stage, both the frequency of AE events and the intensity of energy release showed an abnormally active jump, and the cumulative energy curve presented a steep rising inflection point significantly earlier before it reached the peak stress. This phenomenon highlights that the 200 °C temperature–humidity coupling effect caused in-depth degradation of the concrete's micro-mesoscopic structure (such as severe decomposition of hydration products, extensive debonding at the aggregate–paste interfacial transition zone (ITZ), and pre-existing microcrack networks), which resulted in a substantial reduction in the energy barrier for the material's internal damage accumulation and a significant advance in the critical threshold for unstable propagation of microcracks.

Particularly critical is that the growth rate of post-peak cumulative energy slowed sharply, and even demonstrated a short-term plateau trend, indicating that the crack propagation mode had shifted from the dispersed and progressive failure at room temperature to highly localized rapid penetration, in which the characteristics of the material's brittle fracture intensified significantly.

3.4. Thermal Infrared Test

The thermal infrared test results of the specimens under the normal-temperature condition are shown in Figure 11, those under the 100 °C condition are shown in Figure 12, and those under the 200 °C condition are shown in Figure 13.

As shown in Figure 11, under normal temperature and humidity coupling conditions, the infrared thermal imaging analysis of concrete specimens revealed the typical characteristics of their thermodynamic responses and damage evolution mechanisms. Infrared thermograms indicated that the temperature field on the specimen's surface exhibited significant spatial heterogeneity during uniaxial compression: continuous temperature rises ($\Delta T \approx 1.2$–2.8 °C) occurred in the central region and the contact zone with the upper indenter. This phenomenon resulted from the conversion of elastic energy into thermal energy attributable to stress concentration and frictional heat generation from internal microcracks. The high consistency between the central area in Figure 11c/the corner in Figure 11e and the final failure surface suggested that thermal signals can characterize the damage accumulation process effectively. When the stress approached the peak value (t = 436–441 s), a sudden temperature drop ($\Delta T \approx -3.5$ °C) occurred in the crack initiation

zone. This thermal shock effect stemmed from adiabatic expansion caused by fracture energy release and heat absorption from water vapor evaporation in micro-regions, and confirmed moisture migration's key role in dissipating energy.

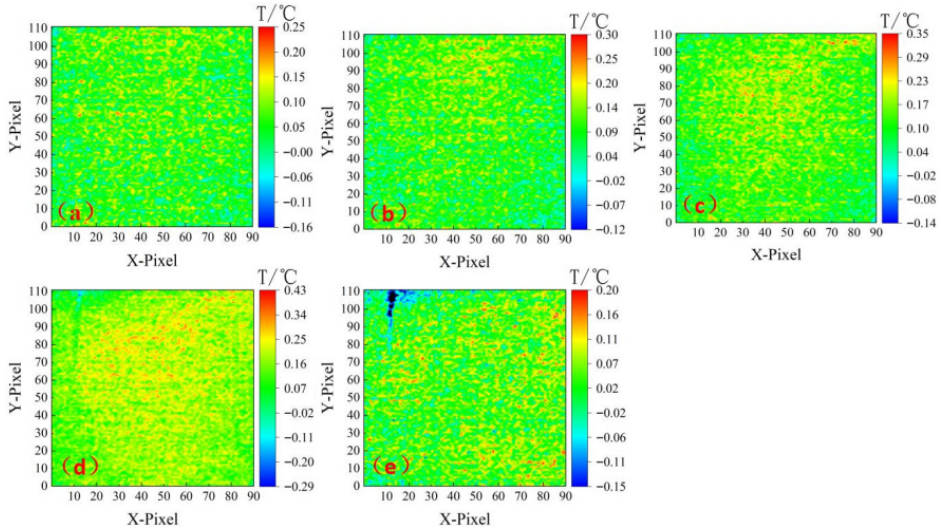

Figure 11. Temperature variation diagram of room-temperature concrete specimens ((**a**) 120 s, (**b**) 220 s, (**c**) 320 s, (**d**) 436 s, (**e**) 441 s).

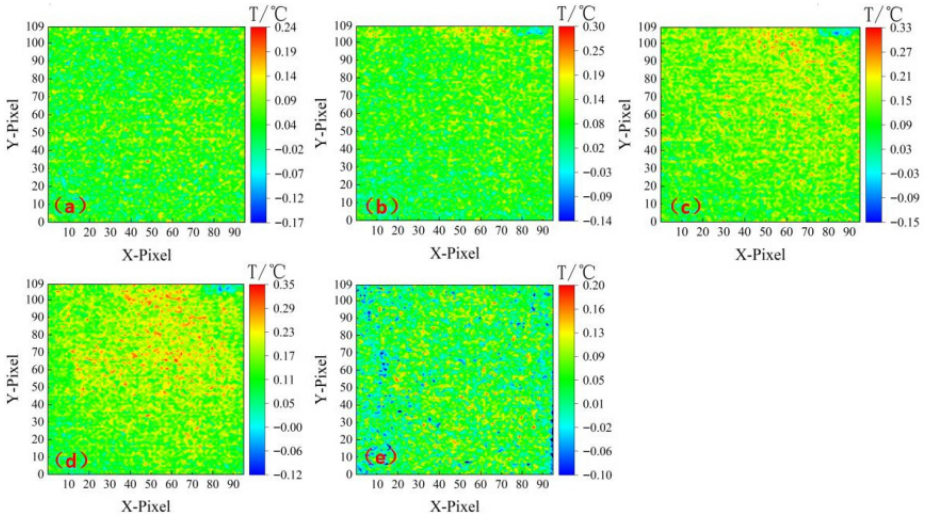

Figure 12. Temperature variation diagram of concrete specimens under 100 °C temperature–humidity coupling ((**a**) 120 s, (**b**) 220 s, (**c**) 320 s, (**d**) 392 s, (**e**) 412 s).

As shown in Figure 12, under the 100 °C temperature–humidity coupling condition, the evolution of the surface temperature field during uniaxial compression revealed by thermograms exhibited three-stage characteristics:

Because of the superposition of the specimen's initial thermal background (~100 °C) and heat generated by compression, in the initial stage (t < 120 s), the temperature rise rate (dT/dt ≈ 0.18 °C/s) overall was significantly higher than that of the specimen under normal temperature.

In the development stage (120–392 s), energy accumulation presented a bimodal distribution—the indenter contact area formed a continuous high-temperature zone attributable to frictional effects (ΔTmax ≈ 4.2 °C), while the central part of the specimen underwent local temperature reduction (ΔTmin ≈ −1.5 °C) caused by pore vapor migration. This thermal differentiation phenomenon stemmed from the strong coupling between the moisture phase change and stress field at high temperatures: the reduction in liquid water

weakened the capillary heat absorption effect, but enhanced vapor diffusion intensified heat loss through convection.

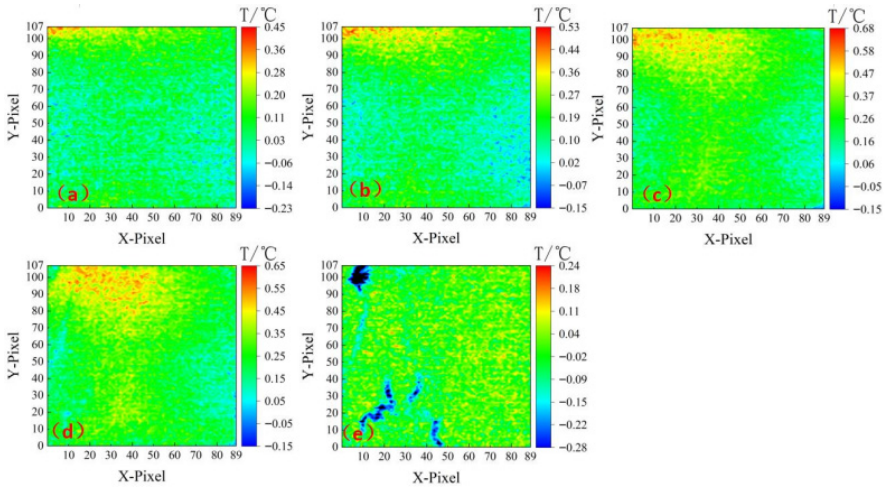

Figure 13. Temperature variation diagram of concrete specimens under 200 °C temperature–humidity coupling ((**a**) 122 s, (**b**) 220 s, (**c**) 320 s, (**d**) 411 s, (**e**) 439 s).

In the failure stage (t > 392 s), crack initiation was accompanied by a severe thermal shock effect ($\Delta T \approx -5.8$ °C), in which the temperature drop amplitude increased by 65% compared to the normal-temperature specimen. This was attributable to the fact that high temperature reduced the energy required for microcrack propagation and enhanced the adiabatic expansion effect of vapor at the crack tip.

The damage mode exhibited obvious high-temperature characteristics: the thermal concentration coefficient in the indenter area (T = 1.85) was 40% higher than that of the normal-temperature specimen, indicating that the contact surface is more prone to shear failure; the spatial consistency between the crack location and the high-temperature core–low-temperature anomaly zone ($|\Delta T| \geq 1.5$ °C/cm) reached 92%, which verified infrared features' sensitive ability to provide an early warning of high-temperature damage.

The temperature–humidity coupling mechanism underwent an essential transformation at this temperature threshold—moisture dominated the heat transport process in the form of vapor migration, and its latent heat of phase change regulated the energy distribution mode significantly. As a result, the thermodynamic response presented composite characteristics: frictional heat generation dominates the temperature rise in the indenter area, vapor diffusion inhibits the temperature rise in the central part, and phase change heat absorption intensifies the temperature drop during fracture.

In the initial stage (t < 220 s) of Figure 13, a high-temperature core was formed preferentially in the indenter area ($\Delta T_{max} \approx 5.8$ °C), where its thermal concentration coefficient (KT = 2.1) increased by 13.5% compared to the 100 °C specimen. This was attributable to the weakened aggregate–mortar interface caused by high temperature, which enhanced the frictional heat effect. In the development stage (220–411 s), energy accumulation exhibited a unique pattern of "migration from the edge to the center" (Figure 13b,c). This phenomenon is related to the micro-pore network formed by the dehydration of cement paste at the threshold of 200 °C; directional migration of pore vapor (flow rate ~0.35 mm/s) induced redistribution of thermal convection and resulted in a bipolar gradient characteristic in the temperature field ($|\Delta T| \geq 2.0$ °C/cm). In the failure stage (t > 430 s), crack initiation was accompanied by intense heat dissipation ($\Delta T \approx -7.2$ °C), in which the temperature drop amplitude increased by 24.1% compared to the 100 °C specimen. The mechanism lays in the fact that high temperature reduced the crack propagation energy to 38% of that at room temperature, and the Joule–Thomson effect of vapor at the crack tip was

enhanced significantly. The damage evolution presented high-temperature brittle characteristics: the spatial correlation between the initial thermal anomaly area (upper left corner/upper indenter) and the final fracture surface reached 95%, while the thermal shock time constant ($\tau \approx 0.6$ s) when the crack forms was shortened to 45% of that of the room-temperature specimen, confirming the phase change-mechanics' coupling mechanism that high-temperature accelerates energy release. The temperature–humidity coupling effect is reconstructed deeply at this temperature: complete vaporization of free water shifted heat transport from capillary action to vapor diffusion dominance. The phase change latent heat (~2200 kJ/kg) and increased permeability ($k \approx 1.8 \times 10^{-14}$ m^2) jointly led to an imbalance in energy distribution among the three processes of indenter frictional heat accumulation, vapor migration heat dissipation, and crack phase change heat absorption; macroscopically, in technical contexts, this represents an increase of 37% in the thermodynamic responses' spatial heterogeneity.

As the temperature–humidity coupling temperature increased, the concrete's thermodynamic behavior showed a significant threshold response. Both the room-temperature and 100 °C specimens exhibited central energy accumulation (thermal concentration coefficient KT = 1.62→1.85), but at 100 °C, the indenter friction temperature increase was enhanced by 40% and the local temperature dropped because of vapor diffusion ($|\Delta T|$ increased to 1.5 °C/cm). At the critical point of 200 °C, the energy accumulation mode transformed into "edge-to-center migration" (Figure 13 (b→c)), which was related to the achievement of the migration of vapor in pores (0.35 mm/s) caused by the micro-pore network formed by cement paste dehydration at 200 °C, which resulted in a bipolar temperature gradient ($|\Delta T| \geq 2.0$ °C/cm). The thermal shock effect in the failure stage strengthened gradually: the temperature drop amplitude in the crack area increased from −3.5 °C (room temperature) to −7.2 °C (200 °C), and the mechanism shifted from capillary heat absorption to vapor adiabatic expansion (Joule–Thomson effect), while the heat absorption efficiency increased by 65%. The ability to warn of early damage was optimized simultaneously: the spatial correlation between thermal anomaly areas and fracture surfaces increased from 86% (room temperature) to 95% (200 °C), and the thermal shock time constant was shortened by 55%. Thus, the temperature–humidity coupling mechanism led to a paradigm shift from liquid capillary action to gaseous vapor diffusion dominance.

4. Conclusions

This study systematically revealed concrete's deformation and catastrophe mechanism under temperature–humidity coupling through an innovative experimental system (100/200 °C constant temperature/water cooling/thermal–humidity shock + DRTB-4000 uniaxial compression test loading) and multi-scale monitoring technologies (synchronous coupling of DIC/AE/infrared). The main conclusions are as follows:

Temperature–humidity coupling induced degradation of mechanical properties and reconstruction of failure modes. High temperature and high humidity weakened the concrete's ductility and strength significantly: the peak strain of the 100 °C/200 °C groups decreased by 30.6% from that at room temperature (0.36%) to 0.25%, and the compressive strength decreased by 2.9%/8.6%. DIC revealed the reconstruction of failure modes: multi-crack progressive expansion at room temperature (strain 0.48%), double-end jump damage at 100 °C (principal strain 0.1%), and directional brittle fracture at 200 °C (strain band 0.015%). The displacement field shifted from shear–tension coupling to one-way separation that resulted from the local concentration of strain energy caused by ITZ weakening.

A reduced micro-damage energy barrier and a forward shift in the brittleness threshold occurred. Acoustic emission monitoring showed that temperature–humidity coupling reduced the energy barrier for microcrack propagation: the cumulative energy of the

200 °C group (4000 mV·ms) was only 2% of that at room temperature (200,000 mV·ms), in which the damage inflection point shifted forward significantly. The non-linear surge of pre-peak AE energy reflected the early instability of damage caused by ITZ weakening; the post-peak energy plateau confirmed that the failure mode shifted from being dispersed and progressive at room temperature to being localized and rapid penetration at high temperature, in which the mechanism was the systematic degradation of fracture toughness.

Heat–force–humidity coupling dominated the energy dissipation and thermal shock strengthening effect. Infrared thermography showed the transformation of the energy dissipation paradigm: "central concentration" temperature increased at room temperature ($\Delta T \approx 1.2$–2.8 °C) followed by "edge-to-center migration" at 200 °C ($|\Delta T| \geq 2.0$ °C/cm), caused by directional migration of steam guided by dehydrated pores. The thermal shock effect in the crack area ($\Delta T \approx -7.2$ °C) was 106% stronger than that at room temperature (-3.5 °C). The mechanism was upgraded from capillary heat absorption to steam phase change latent heat (2200 kJ/kg) and the Joule–Thomson effect, which resulted in the reduction in crack propagation energy to 38% of that at room temperature and accelerated release (time constant reduced by 55%).

The quantitative model of the "strain energy concentration degree–brittleness degradation index" established in this study provides a theoretical tool to assess the safety of concrete structures in high-temperature and high-humidity environments. Key early warning indicators include the one-way separation degree of the displacement field (monitored by DIC), forward shifts in the AE cumulative energy inflection point (>40% indicates brittleness risk), and reversal of infrared temperature gradient ($|\Delta T| > 1.5$ °C/cm marks damage initiation). This achievement is applicable to both designing fire protection and preventing catastrophic failure in concrete structures in harsh environments, such as nuclear power plant containment and undersea tunnels.

Author Contributions: Conceptualization, M.L., C.Z., A.D., X.H., J.L. and X.L.; methodology, M.L., C.Z., A.D., J.L. and X.L.; software, M.L., X.H. and X.L.; validation, M.L., C.Z., A.D., X.H. and X.L.; formal analysis, M.L. and C.Z.; investigation, M.L., C.Z., A.D., X.H. and J.L.; resources, M.L., C.Z., A.D., X.H., J.L. and X.L.; data curation, M.L., C.Z., A.D., J.L. and X.L.; writing—original draft, M.L., A.D., X.H., J.L. and X.L.; writing—review and editing, M.L.; visualization, M.L. and A.D.; supervision, M.L. and A.D.; project administration, M.L. and J.L.; funding acquisition, M.L. All authors have read and agreed to the published version of the manuscript.

Funding: National Natural Science Foundation Youth Fund (42402291).

Data Availability Statement: Data underlying the results presented in this paper are not publicly available at this time but may be obtained from the authors upon reasonable request.

Acknowledgments: The authors gratefully acknowledge the support from the Institute of Defence Engineering AMS, PLA, Luoyang. This work was also supported by the School of Intelligent Construction and Civil Engineering, Luoyang Institute of Science and Technology; the State Key Laboratory of Target Vulnerability Assessment; the Henan Key Laboratory of Special Protective Materials; and the College of Aerospace and Civil Engineering, Harbin Engineering University.

Conflicts of Interest: The authors declare that there are no conflicts of interest related to this article.

References

1. Guo, G.; Ren, S.; Chen, Y. Research Progress on High-Temperature Infrared Stealth Materials. *Mater. Eng.* **2025**, *53*, 45–54.
2. Yang, W.; Hou, L.; Zhang, Y.; Zhang, D. Experimental study on temperature sensitivity of magnetic fluid magnetization. *Transducer Micr. Tech.* **2024**, *43*, 21–24.
3. Gu, Q.; Wang, Y.; Wang, R.; Xie, G. Experimental Study on Early-Age Damage of Mass Concrete under Temperature-Humidity Coupling. *Urban Roads Bridges Flood Control.* **2025**, *1*, 236–243.

4. Wu, Y.; Wang, Z.; Zhou, H.; Zhang, G.; Li, S. Dynamic mechanical properties of high-temperature concrete under different cooling methods. *Explos. Shock Waves* **2025**, *45*, 1–15.
5. Kuang, Y.; Yao, Z.; Bian, H.; Zhao, J.; Li, X.; Zhang, L. Influence of fire extinguishing agents on compressive strength and splitting tensile strength of high-temperature concrete. *J. Zhengzhou Univ. (Eng. Sci.)* **2024**, *45*, 111–116.
6. Yang, H.; Ma, X.; Li, X. The diagnosis of DIC: A current overview. *Front. Med.* **2025**, *12*, 1502628. [CrossRef]
7. Li, Z.; Wang, J.; Li, Y.; Chai, J. Crack propagation law of roller compacted concrete layer based on DIC technology. South-North Water Transf. *Water Sci. Technol.* **2024**, *22*, 987–996.
8. Yan, B.; Kou, Y.; Qin, Y.; Luo, L.; Li, S.; Li, Y. Global identification and reconstruction of concrete structure crack development based on DIC method. *China J. Highw. Transp.* **2024**, *37*, 283–297.
9. Tang, S.; Tang, C.; Lin, G. Review on temperature-humidity coupling effect of concrete. *J. Build. Struct.* **2009**, *30*, 315–318.
10. Zhang, M. Study on Humidity Field Characteristics of Early-Age Concrete in Cold Regions. Master's Thesis, Shenyang Jianzhu University, Shenyang, China, 2022.
11. Li, X. Changes in durability performance of fiber-reinforced concrete under temperature-humidity coupling cyclic action. *New Build. Mater.* **2021**, *48*, 82–84.
12. Zhao, Q.; Yang, T.; Zhang, B.; Zhao, Y.; Teng, L.; Du, S. Failure modes and acoustic emission characteristics of rocks under different fracture dip angles. *J. Min. Sci. Technol.* **2025**, *10*, 203–213.
13. Bai, W.; Li, S.; Guan, J.; Zheng, Y.; Yuan, C. Dynamic mechanical properties of recycled concrete under uniaxial compression. *J. Build. Mater.* **2022**, *25*, 498–508.
14. Pan, X.; Cao, J.; Luo, T.; Tang, L. Precursor characteristics of uniaxial compression failure of early-age steel fiber reinforced concrete. *Bull. Chin. Ceram. Soc.* **2024**, *43*, 2470–2478.
15. Wu, J.; Li, H.; Ma, D.; Wang, C. Multifractal characteristics of surface crack distribution of concrete under uniaxial compression. *Chin. Q. Mech.* **2023**, *44*, 904–913.
16. Li, Q.; Li, Q.; Gao, Y.; Li, Z. Damage evolution and acoustic emission analysis of concrete during uniaxial compression. *J. Shenyang Univ. Technol.* **2020**, *42*, 687–693.
17. Yu, P.; Duan, Y.; Fan, Q.; Tang, S. Improved MPS model for concrete creep under variable humidity and temperature. *Constr. Build. Mater.* **2020**, *243*, 118183. [CrossRef]
18. Wang, L.; Zhao, Y.; Guo, J.; Zhang, J. Acoustic emission characteristics of uniaxial failure of concrete and its constituent materials. *J. Civ. Environ. Eng.* **2025**, *47*, 174–181.
19. Wu, C.; Yang, J.; Li, Q. Damage characteristics of concrete under compression based on acoustic emission technology. *J. Vib. Meas. Diagn.* **2024**, *44*, 608–613.
20. Shao, Z.; Zhang, G.; Li, C.; Niu, H.; Gao, B. Experimental study on humidity response of concrete under different atmospheric temperature and humidity conditions. *Concr. Cem. Prod.* **2023**, *8*, 31–36.
21. Yoon, M.; Kim, G.; Kim, Y.; Lee, T.; Choe, G.; Hwang, E.; Nam, J. Creep behavior of high-strength concrete subjected to elevated temperatures. *Materials* **2017**, *10*, 781. [CrossRef]
22. Yu, A. Study on Moisture Migration Behavior of Large-Void Asphalt Concrete Under Hygrothermal Conditions. Master's Thesis, Nanjing Forestry University, Nanjing, China, 2023.
23. Biswal, S.; Reddy, D.; Ramaswamy, A. Reducing uncertainties in estimating long-time prestress losses in concrete structures using a hygro-thermo-chemo-mechanical model for concrete. *Comput. Struct.* **2019**, *211*, 1–13. [CrossRef]
24. Lyu, C.; Xu, M.; Lu, X.; Tian, B.; Chen, B.; Xiong, B.; Chen, B. Research on thermal-humidity-force coupling characteristics of mass concrete structures under temperature control. *Constr. Build. Mater.* **2023**, *398*, 132456. [CrossRef]
25. Chen, D.; Zou, J.; Zhao, L. Degradation of dynamic elastic modulus of concrete under periodic temperature-humidity action. *Materials* **2020**, *13*, 611. [CrossRef] [PubMed]
26. Min, H.; Zhang, W.; Gu, X.; Černý, R. Coupled heat and moisture transport in damaged concrete under an atmospheric environment. *Constr. Build. Mater.* **2017**, *143*, 607–620. [CrossRef]
27. Qin, M.; Belarbi, R.; Aït-Mokhtar, A.; Nilsson, L.-O. Coupled heat and moisture transfer in multi-layer building materials. *Constr. Build. Mater.* **2009**, *23*, 967–975. [CrossRef]
28. You, W.; Wang, Y.; Zhang, X.; Xu, G.; Wang, S. Calculation of temperature-humidity coupling stress and cracking risk analysis of high-strength concrete. *J. Harbin Inst. Technol.* **2017**, *49*, 170–175.
29. Shu, H.; Yin, W.; Wang, C.; Liu, S.; Wang, Y. Experimental study on pore structure and strength of shotcrete under temperature-humidity coupling action. *Tunn. Constr.* **2020**, *40*, 1700–1708.
30. Li, X.; Shen, A. Study on internal stress of pavement concrete under temperature-humidity coupling action. *J. Build. Mater.* **2018**, *21*, 78–84. [CrossRef]
31. Wang, X.; Zhang, Y.; Li, Z. Influence of temperature-humidity warping on reinforcement design of continuously reinforced concrete pavement. *J. Highw. Transp. Res. Dev.* **2021**, *38*, 33–40.

32. Lu, X.; Shuang, N.; Chen, B.; Yin, G.; Liu, X. Evolution law and driving mechanism of internal temperature and humidity of mass concrete under variable temperature conditions. *Yellow River* **2023**, *45*, 146–150.
33. Zheng, W.; Fen, Z. Study on thermal and humidity properties of new light steel keel composite wall. *J. Beijing Univ. Chem. Technol. (Nat. Sci.)* **2024**, *51*, 61–70.

Disclaimer/Publisher's Note: The statements, opinions and data contained in all publications are solely those of the individual author(s) and contributor(s) and not of MDPI and/or the editor(s). MDPI and/or the editor(s) disclaim responsibility for any injury to people or property resulting from any ideas, methods, instructions or products referred to in the content.